

Science

 AAAS

Self-Sorted, Aligned Nanotube Networks for Thin-Film Transistors

Melburne C. LeMieux, *et al.*

Science **321**, 101 (2008);

DOI: 10.1126/science.1156588

The following resources related to this article are available online at www.sciencemag.org (this information is current as of July 10, 2008):

Updated information and services, including high-resolution figures, can be found in the online version of this article at:

<http://www.sciencemag.org/cgi/content/full/321/5885/101>

Supporting Online Material can be found at:

<http://www.sciencemag.org/cgi/content/full/321/5885/101/DC1>

A list of selected additional articles on the Science Web sites **related to this article** can be found at:

<http://www.sciencemag.org/cgi/content/full/321/5885/101#related-content>

This article **cites 27 articles**, 5 of which can be accessed for free:

<http://www.sciencemag.org/cgi/content/full/321/5885/101#otherarticles>

This article appears in the following **subject collections**:

Physics, Applied

http://www.sciencemag.org/cgi/collection/app_physics

Information about obtaining **reprints** of this article or about obtaining **permission to reproduce this article** in whole or in part can be found at:

<http://www.sciencemag.org/about/permissions.dtl>

Self-Sorted, Aligned Nanotube Networks for Thin-Film Transistors

Melburne C. LeMieux,¹ Mark Roberts,¹ Soumendra Barman,¹ Yong Wan Jin,² Jong Min Kim,² Zhenan Bao^{1*}

To find use in electronics, single-walled carbon nanotubes need to be efficiently separated by electronic type and aligned to ensure optimal and reproducible electronic properties. We report the fabrication of single-walled carbon nanotube (SWNT) network field-effect transistors, deposited from solution, possessing controllable topology and an on/off ratio as high as 900,000. The spin-assisted alignment and density of the SWNTs are tuned by different surfaces that effectively vary the degree of interaction with surface functionalities in the device channel. This leads to a self-sorted SWNT network in which nanotube chirality separation and simultaneous control of density and alignment occur in one step during device fabrication. Micro-Raman experiments corroborate device results as a function of surface chemistry, indicating enrichment of the specific SWNT electronic type absorbed onto the modified dielectric.

The combination of superior electrical and mechanical properties in single-walled carbon nanotubes (SWNTs) (1, 2) continues to advance applications, including flexible electronics (3, 4), biosensors and biochemical sensors (5), and solar cell technology (6). Despite enormous progress toward the potential applied uses of SWNT devices, such applications will not be realized unless fundamental issues concerning the controlled reproducible placement, alignment, and separation based on chirality and/or diameter can be solved.

Accurate orientation of SWNTs has been achieved from high-temperature growth (7), and on a limited scale, at ambient conditions with diverse approaches including dielectrophoresis (8), gas-flow (9), evaporating droplet (10, 11), and absorption affinity patterns (12, 13). As a more realistic route for integration, researchers have recently turned to random nanotube networks that are easily absorbed or deposited from solution to form two-dimensional (2D) nanotube films (4, 9, 14, 15) as the active semiconducting layer in SWNT network thin-film transistors (Fig. 1A). However, these devices suffer from poor on/off ratios due to the presence of both semiconducting and metallic tubes intrinsic to all SWNT synthesis methods. Although metallic SWNTs may serve as high-performance interconnects (16), they lead to high off current and shorted transistors. The metallic SWNTs may be burned off after fabrication (17), but this additional processing step is neither well controlled nor scalable.

Our goal is to move beyond random nanotube films to submonolayer SWNT networks with

controlled topology in which chirality, alignment, and density may be tuned or sorted, ideally during fabrication. We took SWNT solutions and spincoated them onto piranha-cleaned silicon wafers with a 300-nm dry thermal oxide (18) modified with various silane monolayers chosen

for their relative ease of surface modification and the variety of chemical functional groups available (Fig. 1). Independent of the solvent volatility used for deposition, if the SWNT solution is spincoated on bare (unmodified) SiO₂, no nanotube absorption occurs. To control absorption characteristics, we functionalized the SiO₂ dielectric surface with amine- and phenyl-terminated silanes (Fig. 1). The thickness of the amine and phenyl surfaces, measured by ellipsometry, was 0.7 and 0.4 nm, respectively, and root mean square (RMS) surface roughness (19) did not exceed 0.2 nm (table S1), indicating uniform monolayers.

Aminosilanes are used because they enhance the absorption of nanotubes (20) and improve the performance of isolated SWNT thin-film transistors (TFTs) as sensors (21). Furthermore, the pioneering work by Papadimitrakopoulos has shown selective absorption of amines toward semiconducting SWNTs (22, 23). However, theory (24) and experiment (25) have shown that aromatic molecules like the phenyl-terminated silane used here interact and bind selectively to metallic SWNTs. The selectivity is attributed to the fact that SWNTs are extended π -electron systems that can interact with other π -electron systems via π - π stacking. This is expected to be stronger with the metallic nanotubes because of a

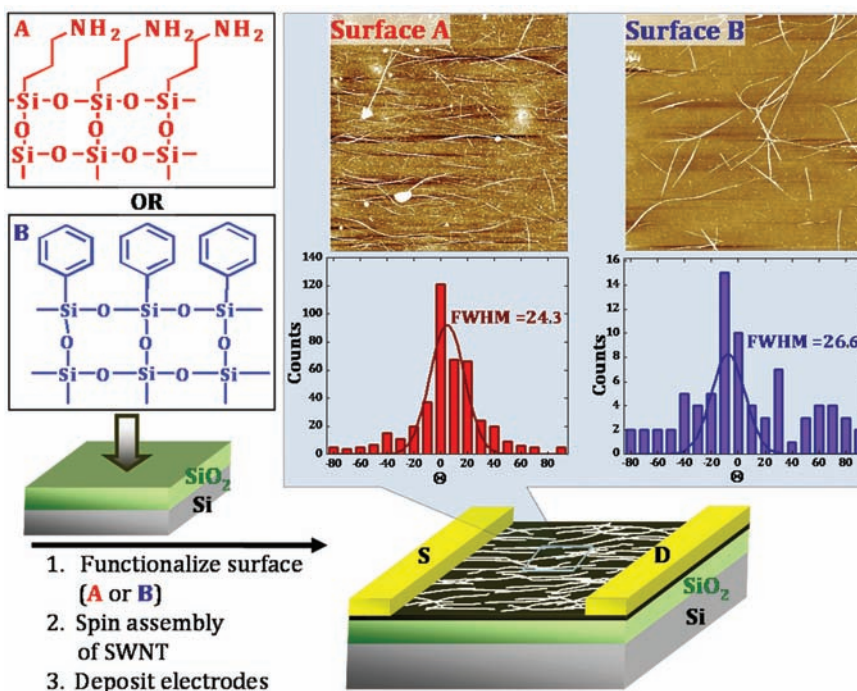


Fig. 1. Schematic of the SWNT TFT fabrication and structure. The dielectric (300-nm SiO₂ on a heavily doped Si gate) is functionalized by either an amine-terminated (A) or phenyl-terminated (B) silane. The SWNT solution is subsequently dispensed onto the spinning self-assembled monolayer-modified substrate and dried, followed by source (S) and drain (D) gold electrode deposition. Shown here is the top-contact device structure, although similar results are obtained in bottom-contact layouts where source and drain electrodes are deposited before spin assembly of the nanotubes. Upon spincoating, AFM tapping-mode topography images (10 μ m by 10 μ m, z scale = 10 nm) of the nanotubes applied under identical conditions on amine (top) and phenyl (bottom) surfaces reveals that density and alignment, represented by histogram (Θ is angle, in degrees, of variation from an arbitrary direction) below the corresponding AFM images, are a direct function of surface chemistry.

¹Department of Chemical Engineering, Stanford University, Stanford, CA 94305, USA. ²Samsung Advanced Institute of Technology, Giheung-gu, Younggin-si Gyunggi-do 449-712, South Korea.

*To whom correspondence should be addressed. E-mail: zbao@stanford.edu

larger polarizability relative to the semiconducting nanotubes (8). An unresolved question, especially relevant for device applications, is whether this selectivity can be translated to interactions at surfaces.

Qualitatively, spincoating the SWNT solution on the various silane-treated surfaces under the same conditions resulted in the tube density being substantially modulated by surface chemistry. As determined from atomic force microscopy (AFM) images (10 μm by 10 μm) (Fig. 1) taken at random locations on the wafer (except at the center of the wafer), the absorption density of the isolated SWNT was higher on aminosilanes (8 to 10 per μm^2) than on the phenyl surfaces (1 to 2 per μm^2). This is expected on the basis of simulation results (24) that found that the highest equilibrium absorption energy of an NH_2 group with SWNTs, regardless of chirality, is 0.57 eV, almost three times as strong as that of phenyl groups, which is ~ 0.20 eV. Upon spincoating, the average alignment over the entire wafer (2.5 cm), as measured by AFM images (10 μm by 10 μm) (Fig. 1), indicates that at any location, $\sim 71\%$ of the SWNTs are aligned within $\pm 10\%$ of an arbitrary axis, with a slightly higher degree of alignment observed on the amine surface as compared to the phenyl surface (histograms in Fig. 1). The hydrodynamic flow, which has been shown to efficiently align nanoparticles on a drying surface (26), appears to be markedly enhanced by the spinning wafer and effectively aligns the nanotubes as the solvent evaporates and thins (10). The degree of alignment can be tuned on the basis of spin-assembly conditions (fig. S1). The alignment is radial from the center, with the only unaligned area being the portion concentric with the vacuum chuck on the spin coater (~ 2 mm in diameter on a 12.7-mm-diameter wafer) (fig. S2). No alignment was observed when the SWNTs were deposited by wafer soaking or dropping the solution followed by spinning (fig. S3). Spincoating conditions (volume, rate) could be controlled so that nearly the same SWNT density was absorbed onto amine and phenyl surfaces for comparing the resulting electronic and micro-Raman spectroscopy analysis.

To determine whether and how different surface functionalities affect the electronic response of the SWNT thin-film transistors, we performed electronic testing and micro-Raman mapping in the channel region of the TFTs over random substrate locations. The SWNT TFTs on aminosilane surfaces exhibit p-type behavior with on/off ratios as high as 900,000 and without any post-processing or device level burn-off (17), indicating that the nanotube network is composed primarily of semiconducting nanotubes (Fig. 2, A and B). The average on/off ratio for working devices was $\sim 200,000$, and leakage current was in the picoamp range with no dependence on applied gate voltage. Field-effect mobility (27) of the TFTs on amine surfaces ranged from ~ 0.5 to $6 \text{ cm}^2/\text{V}\cdot\text{s}$ (fig. S4). Overall, 38% of the 80 devices tested on amine surfaces had on/off ratios

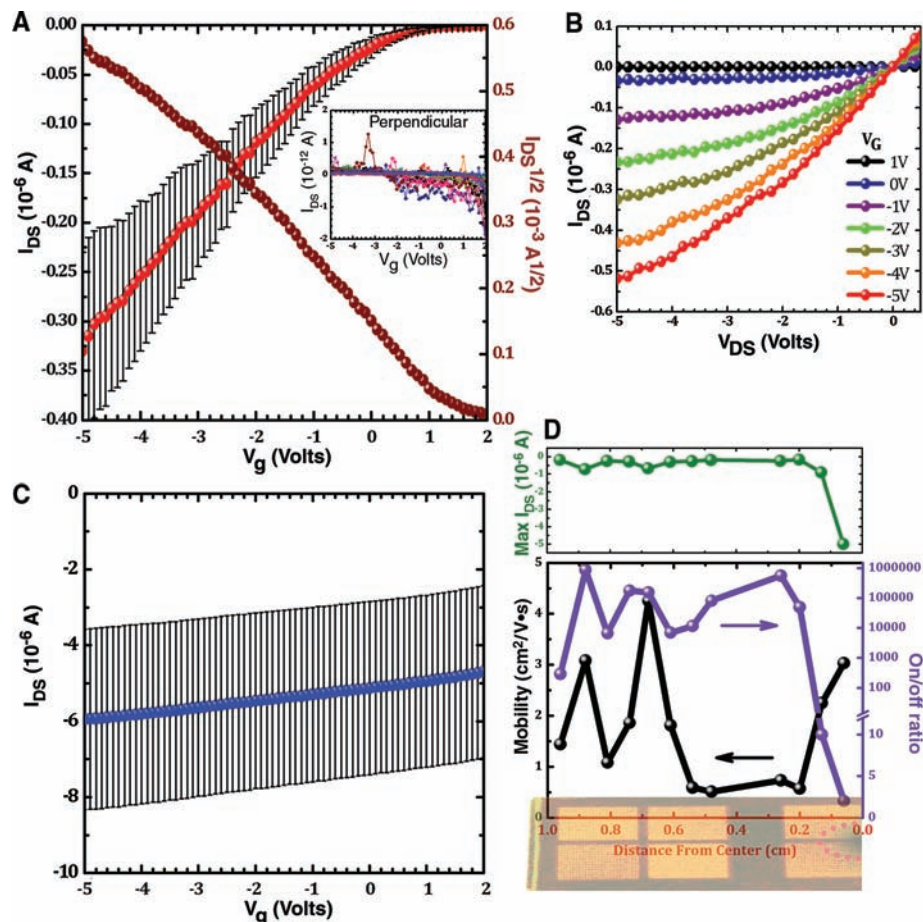


Fig. 2. (A) Plot of all measured devices showing the mean \pm SD of source/drain current (I_{DS}) as a function of gate voltage (V_G) for SWNT TFTs on an amine-terminated surface showing high on/off ratio in devices with current-flow direction parallel to hydrodynamic flow direction. Because the hydrodynamic flow is radial from the center of the substrate during spincoating, the working devices have current-flow primarily along this direction. Perpendicular to flow, the devices are insulating because a percolating network is suppressed (inset). (B) Typical plot of I_{DS} as a function of V_G for the SWNT TFT on amine-terminated surfaces. A slightly positive threshold ($V_T \sim 0.7$ V) is associated with the transistors as a result of oxygen doping. (C) Plot of all measured devices showing the mean \pm SD of I_{DS} as a function of V_G for SWNT TFTs on phenyl surfaces showing a high “off” current and a low on/off ratio. Error bars in (A) and (C) represent the SD in the transfer curves. (D) Uniformity of the spin-assisted assembly method over a ~ 2 -cm bottom-contact device substrate demonstrating scalability. The plot is superimposed on a device wafer (digital image) with the highlighted shaded circle indicating high (uncontrollable) concentration of SWNTs that is found only in the very center of the wafer (see supporting online material). The top plot represents the maximum “on-current” for one typical wafer, and the bottom plot compares mobility and on/off ratio as a function of test location on the wafer.

of $>100,000$, 69% had ratios of $>10,000$, and more than 95% had ratios of >100 on bottom and top contact devices possessing a channel length of $\geq 15 \mu\text{m}$ (18). Even at a smaller channel length of 10 μm , an average on/off ratio approaching 10,000 was maintained (fig. S5). Although amines can slightly modulate SWNT doping levels, the on/off ratio is not affected (21). Similarly, we confirmed that the high on/off ratios were not due to dedoping by amine groups, because the drop-and-spin samples with the same SWNT density on the amine surface showed no selectivity and a low on/off ratio (fig. S3).

SWNT TFTs fabricated on the aromatic surfaces with the same density, however, always led to conducting devices, and all devices had on/off

ratios of less than ~ 2 , indicating that the phenyl surfaces are dominated by metallic nanotubes. Figure 2C shows the averaged transfer curve. The resulting error bars are relatively high due to different levels of “off-current” that averaged around -6.0×10^{-6} , which are five to six orders of magnitude higher than those of the off-current on the amine surfaces. Furthermore, the overall higher source/drain current (I_{DS}) maximum “on current” for the phenyl surfaces, as opposed to the amine surfaces, may be another indication that the phenyl surfaces are dominated by metallic nanotubes because of the higher current-carrying capacity. This pronounced difference in the electronic nature of the SWNT networks on the two surfaces is observed down to very short

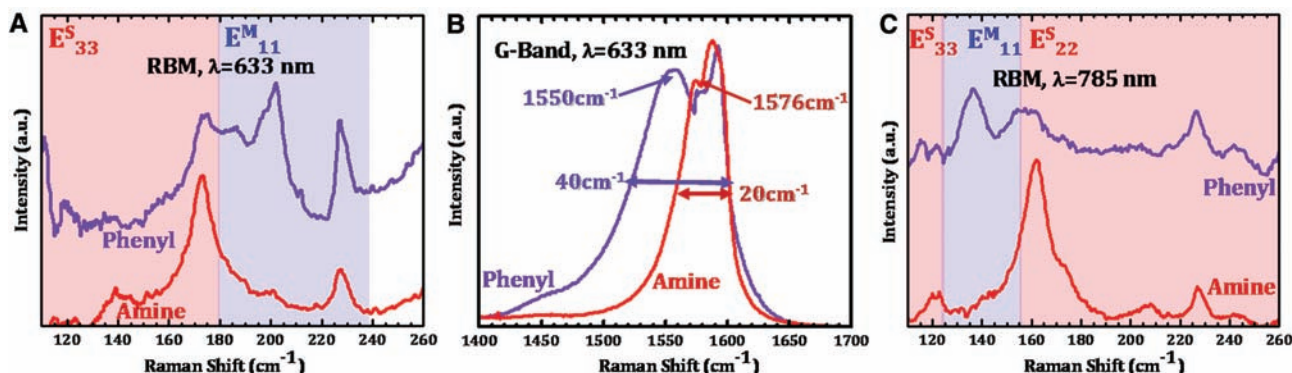


Fig. 3. (A) Micro-Raman spectra at 1.96-eV excitation showing RBMs compiled from 12 point maps from at least five different locations of the SWNT network on each surface. All spectra shown here were normalized to the 303-cm⁻¹ silicon peak; the peaks below 120 cm⁻¹ result from noise, whereas the peak at ~225 cm⁻¹ arises from silicon. (B) Corresponding G-band compilations at 1.96 eV of each surface shows a marked downshift and broadening of ω_G -band from the SWNTs on the

phenyl surface (blue trace) resulting from metallic SWNTs as compared to the amine surface (red trace). The full width at half-maximum of the G⁻ band is twice as high on the phenyl surface as compared to the amine surface. (C) Raman spectra at 1.58-eV excitation showing RBMs compiled from each surface. The phenyl surface (blue trace) is enriched with metallic nanotubes, whereas the amine surface (red trace) is enriched with semiconducting nanotubes.

channel lengths of 2 μm , approaching the length of the SWNTs in this study and indicating a high degree of separation (fig. S6).

To identify tube types (28, 29) absorbed on each surface, we performed micro-Raman mapping over large areas of each sample surface in device channels by using two excitation energies and correlating observed resonant radial breathing modes (RBMs) with chirality using a Kataura plot and a relation between diameter and RBM developed by Dresselhaus *et al.* for isolated SWNTs on SiO₂ (29). We used 1.96- and 1.58-eV excitation because most SWNT tubes in this work had a relatively large average diameter but narrow distribution (1.4 ± 0.4 nm as determined by AFM), and should be resonant at these energies. The diameter distribution of arc-discharge nanotubes is known to be quite narrow, more so than that of tubes produced by HiPco and chemical vapor deposition (30), allowing this multi-excitation micro-Raman experiment to be highly reliable and thorough. In particular, the 1.96-eV line is resonant with metallic SWNTs (E_{11}^M) and semiconducting SWNTs (E_{33}^S) in a nearly 50/50 ratio (Fig. 3A) and is best suited for separation analysis.

RBM analysis (Fig. 3A and figs. S7, S8, and S10) from compiled spectra shows that tubes absorbed on both surfaces possess the 170-cm⁻¹ peak because this corresponds to the average diameter of our arc-discharge SWNTs (fig. S5) (31). However, this semiconducting band is clearly much stronger on the amine surface, indicating enrichment of these tubes on amine, as is the 145-cm⁻¹ semiconducting peak that is also observed in the reference sample (fig. S7), but completely suppressed in the nanotube network absorbed on the phenyl surface (Fig. 3A).

In contrast, there is strong enrichment of the 200-cm⁻¹ peak corresponding to metallic SWNTs on the phenyl surface that is nearly nonexistent on the amine surface. Moreover, the 190-cm⁻¹ (metallic band) peak on the phenyl surface, nearly identical in intensity to the 170-cm⁻¹ peak, was

almost completely eliminated from the amine surface. The corresponding G band (Fig. 3B and figs. S9 and S11) from the nanotube network on each surface differs substantially, indicating that the electronic nature of the absorbed nanotubes is very different. Whereas the amine is characterized by two (G^+ and G^-) relatively sharp peaks, on the phenyl surfaces, there is a strong downshift of the G⁻ band accompanied with a distinct Breit-Wigner-Fano line shape characterized by a marked broadening of this same band (Fig. 3B). This downshift and pronounced broadening of the G⁻ band indicate a strong metallic contribution, and along with the markedly higher integrated area G^-/G^+ ratio on the phenyl surfaces, are further evidence for a higher ratio of metallic SWNTs on the phenyl surfaces (Fig. 3B). Thus, micro-Raman experiments corroborate the electronic measurements and explain the huge difference in the electrical response of the sorted nanotube network on each surface. RBM analysis from the 1.58-eV line (Fig. 3C) further reinforces this finding because the amine surface is dominated by the 163-cm⁻¹ peak (E_{22}^S), whereas the phenyl surface has a strong 134-cm⁻¹ peak that corresponds to metallic nanotubes and is highly suppressed on the amine surface.

By spincoating solutions of SWNTs onto functionalized surfaces, we can obtain thin-film transistors with average on/off ratios of $>100,000$. To consistently achieve such high values from a one-step solution-processed SWNT network TFT without any burnoff or additional processing represents a major step toward the application of nanotube electronics. AFM, electronic, and micro-Raman measurements show that the alignment, density, electronic nature, and chirality of SWNTs can be tuned through careful selection of surface functional groups and the spin-assisted assembly described here.

References and Notes

1. R. H. Baughman, A. A. Zakhidov, W. A. de Heer, *Science* **297**, 787 (2002).

2. J. T. Hu, T. W. Odom, C. M. Lieber, *Acc. Chem. Res.* **32**, 435 (1999).
3. J.-H. Ahn *et al.*, *Science* **314**, 1754 (2006).
4. G. Grüner, *J. Mater. Chem.* **16**, 3533 (2006).
5. E. S. Snow, F. K. Perkins, J. A. Robinson, *Chem. Soc. Rev.* **35**, 790 (2006).
6. M. W. Rowell *et al.*, *Appl. Phys. Lett.* **88**, 233506 (2006).
7. C. Kocabas *et al.*, *Nano Lett.* **7**, 1195 (2007).
8. R. Krupke, F. Henrich, H. V. Lohneysen, M. M. Kappes, *Science* **301**, 344 (2003).
9. M. D. Lay, J. P. Novak, E. S. Snow, *Nano Lett.* **4**, 603 (2004).
10. R. Duggal, F. Hussain, M. Pasquali, *Adv. Mater.* **18**, 29 (2006).
11. V. V. Tsukruk, H. Ko, S. Peleshanko, *Phys. Rev. Lett.* **92**, 065502 (2004).
12. S. G. Rao, L. Huang, W. Setyawan, S. Hong, *Nature* **425**, 36 (2003).
13. Y. Wang *et al.*, *Proc. Natl. Acad. Sci. U.S.A.* **103**, 2026 (2006).
14. E. Artukovic, M. Kaempgen, D. S. Hecht, S. Roth, G. Grüner, *Nano Lett.* **5**, 757 (2005).
15. E. S. Snow, J. P. Novak, P. M. Campbell, D. Park, *Appl. Phys. Lett.* **82**, 2145 (2003).
16. P. Avouris, Z. Chen, V. Perebeinos, *Nat. Nanotechnol.* **2**, 605 (2007).
17. P. G. Collins, M. S. Arnold, P. Avouris, *Science* **292**, 706 (2001).
18. Materials and methods are available as supporting material on Science Online
19. Surface roughness measured by tapping-mode AFM was calculated over at least five different areas (1 μm by 1 μm) on the samples.
20. J. Liu *et al.*, *Chem. Phys. Lett.* **303**, 125 (1999).
21. S. Avoury *et al.*, *Nano Lett.* **5**, 451 (2005).
22. D. Chattopadhyay, L. Galeska, F. A. Papadimitrakopoulos, *J. Am. Chem. Soc.* **125**, 3370 (2003).
23. Although it has been shown by simulation only [see, for example, (22)] that NH₂ may selectively interact with neutral metallic nanotubes more favorably than with neutral semiconducting nanotubes, this trend is reversed by oxidation (such as at defect locations), as has been verified experimentally (22, 24). Because all SWNT systems will have some level of defects [and as evidenced by the D' band in micro-Raman spectra (figs. S9 and S11)], it is reasonable to expect that NH₂ should interact more strongly with semiconducting SWNTs in our system.
24. J. Lu *et al.*, *Small* **3**, 1566 (2007).
25. A. Nish, J.-Y. Hwang, J. Doig, R. J. Nicholas, *Nat. Nanotechnol.* **2**, 640 (2007).
26. R. Sharma, C. Y. Lee, J. H. Choi, K. Chen, M. S. Strano, *Nano Lett.* **7**, 2693 (2007).
27. This is calculated as broad mobility that accounts for full electrode width. The actual number of nanotubes

interfacing with the electrodes was not counted for all of these devices.

28. M. S. Dresselhaus, G. Dresselhaus, A. Jorio, A. G. Souza Filho, R. Saito, *Carbon* **40**, 2043 (2002).
29. A. Jorio *et al.*, *Phys. Rev. Lett.* **86**, 1118 (2001).
30. B. Zhao *et al.*, *J. Nanosci. Nanotechnol.* **4**, 995 (2004).
31. S. M. Keogh *et al.*, *J. Phys. Chem. B* **108**, 6233 (2004).
32. This research was partially supported by the NSF-sponsored Center for Polymer Interface and

Macromolecular Assemblies (CPIMA), Samsung Advanced Research Institute of Technology, Intel, and Applied Materials. M.C.L. acknowledges support from the Intelligence Community Postdoctoral Fellowship Program. M.R. acknowledges support from the NASA Graduate Student Research Fellowship. Z.B. acknowledges support from the Sloan Research Fellowship and Finmeccanica Faculty Scholar Award. We thank S. Hellstrom, H. W. Lee, J. N. Kurtin (Intel), and B. Chen (NASA Ames) for technical discussions.

Supporting Online Material

www.sciencemag.org/cgi/content/full/321/5885/101/DC1
Materials and Methods
Figs. S1 to S11
Table S1
References

18 February 2008; accepted 29 May 2008
10.1126/science.1156588

Relativistic Spin Precession in the Double Pulsar

Rene P. Breton,^{1*} Victoria M. Kaspi,¹ Michael Kramer,² Maura A. McLaughlin,^{3,4} Maxim Lyutikov,⁵ Scott M. Ransom,⁶ Ingrid H. Stairs,⁷ Robert D. Ferdman,^{7,8} Fernando Camilo,⁹ Andrea Possenti¹⁰

The double pulsar PSR J0737–3039A/B consists of two neutron stars in a highly relativistic orbit that displays a roughly 30-second eclipse when pulsar A passes behind pulsar B. Describing this eclipse of pulsar A as due to absorption occurring in the magnetosphere of pulsar B, we successfully used a simple geometric model to characterize the observed changing eclipse morphology and to measure the relativistic precession of pulsar B's spin axis around the total orbital angular momentum. This provides a test of general relativity and alternative theories of gravity in the strong-field regime. Our measured relativistic spin precession rate of $4.77^{+0.66}_{-0.65}$ per year (68% confidence level) is consistent with that predicted by general relativity within an uncertainty of 13%.

Spin is a fundamental property of most astrophysical bodies, making the study of its gravitational interaction an important challenge (*1*). Spin interaction manifests itself in different forms. For instance, we expect the spin of a compact rotating body in a binary system with another compact companion to couple gravitationally with the orbital angular momentum (relativistic spin-orbit coupling) and also with the spin of this companion (relativistic spin-spin coupling) (*2, 3*). Observing such phenomena provides important tests for theories of gravity, because every successful theory must be able to describe the couplings and to predict their observational consequences. In a binary system consisting of compact objects such as neutron stars, one can generally consider the spin-orbit contribution acting on each body to dominate greatly the spin-

spin contribution. This interaction results in a precession of the bodies' spin axis around the orbital angular momentum of the system, behavior we refer to as relativistic spin precession.

Although relativistic spin precession is well studied theoretically in general relativity (GR), the same is not true of alternative theories of gravity, and hence quantitative predictions of deviations from GR spin precession do not yet exist (*4*). For instance, it is expected that in alternative theories relativistic spin precession may depend on strong self-gravitational effects; that is, the actual precession may depend on the structure of a gravitating body (*4*). In the weak gravitational fields encountered in the solar system, these strong-field effects generally cannot be detected (*5–7*). Measurements in the strong-field regime near massive and compact bodies such as neutron stars and black holes are required. Relativistic spin precession has been observed in some binary pulsars [e.g., (*8–10*)], but it has usually only provided a qualitative confirmation of the effect. Recently, the binary pulsar PSR B1534+12 allowed the first quantitative measurement of this effect in a strong field, and although the spin precession rate was measured to low precision, it was consistent with the predictions of GR (*11*).

Here, we report a precision measurement of relativistic spin precession using eclipses observed in the double pulsar (*12, 13*). This measurement, combined with observational access to both pulsar orbits in this system, allows us to constrain quantitatively relativistic spin precession in the

strong-field regime within a general class of gravitational theories that includes GR.

PSR J0737–3039A/B consists of two neutron stars, both visible as radio pulsars, in a relativistic 2.45-hour orbit (*12, 13*). High-precision timing of the pulsars, having spin periods of 23 ms and 2.8 s (hereafter called pulsars A and B, respectively), has already proven to be the most stringent test bed for GR in the strong-field regime (*14*) and enables four independent timing tests of gravity, more than any other binary system.

The orbital inclination of the double pulsar system is such that we observe the system almost perfectly edge-on. This coincidence causes pulsar A to be eclipsed by pulsar B at pulsar A's superior conjunction (*13*). The modestly frequency-dependent eclipse duration, about 30 s, corresponds to a region extending $\sim 1.5 \times 10^7$ m (*15*). The light curve of pulsar A during its eclipse shows flux modulations that are spaced by half or integer numbers of pulsar B's rotational period (*16*). This indicates that the material responsible for the eclipse corotates with pulsar B. The relative orbital motions of the two pulsars and the rotation of pulsar B thus allow a probe of different regions of pulsar B's magnetosphere in a plane containing the line of sight and the orbital motion.

Synchrotron resonance with relativistic electrons is the most likely mechanism for efficient absorption of radio emission over a wide range of frequencies. In the model proposed by Lyutikov and Thompson (*17*), this absorbing plasma corotates with pulsar B and is confined within the closed field lines of a magnetic dipole truncated by the relativistic wind of pulsar A. The dipole magnetic moment vector makes an angle α with respect to the spin axis of pulsar B, whose orientation in space can be described by two angles: the colatitude of the spin axis with respect to the total angular momentum of the system, θ , and the longitude of the spin axis, ϕ (see Fig. 1 for an illustration of the system geometry). Additional parameters characterizing the plasma opacity, μ ; the truncation radius of the magnetosphere, R_{mag} ; and the relative position of pulsar A with respect to the projected magnetosphere of pulsar B, z_0 , are also included in the model (*17*).

We monitored the double pulsar from December 2003 to November 2007 with the Green Bank Telescope in West Virginia; most of the data were acquired as part of the timing ob-

¹Department of Physics, McGill University, Montreal, QC H3A 2T8, Canada. ²Jodrell Bank Observatory, University of Manchester, Manchester M13 9PL, UK. ³Department of Physics, West Virginia University, Morgantown, WV 26506, USA. ⁴National Radio Astronomy Observatory, Green Bank, WV 24944, USA. ⁵Department of Physics, Purdue University, West Lafayette, IN 47907, USA. ⁶National Radio Astronomy Observatory, Charlottesville, VA 22903, USA. ⁷Department of Physics and Astronomy, University of British Columbia, Vancouver, BC V6T 1Z1, Canada. ⁸Laboratoire de Physique et Chimie de l'Environnement-CNRS, F-45071 Orleans cedex 2, France. ⁹Columbia Astrophysics Laboratory, Columbia University, New York, NY 10027, USA. ¹⁰Osservatorio Astronomico di Cagliari, Istituto Nazionale di Astrofisica, Poggio dei Pini, 09012 Capoterra, Italy.

*To whom correspondence should be addressed. E-mail: bretonr@physics.mcgill.ca